Breakdown of linear spin-wave theory and existence of spinon bound states in the frustrated kagome-lattice antiferromagnet

K. Matan [1,2,*] T. Ono [3] S. Ohira-Kawamura [4] K. Nakajima,[4] Y. Nambu [5,6,7] and T. J. Sato [8]

[1]*Department of Physics, Faculty of Science, Mahidol University, Bangkok 10400, Thailand*
[2]*ThEP, Commission of Higher Education, Bangkok 10400, Thailand*
[3]*Department of Physical Science, School of Science, Osaka Prefecture University, Sakai, Osaka 599-8531, Japan*
[4]*Materials and Life Science Division, J-PARC Center, Tokai, Ibaraki 319-1195, Japan*
[5]*Institute for Materials Research, Tohoku University, Sendai 980-8577, Japan*
[6]*FOREST, Japan Science and Technology Agency, Kawaguchi, Saitama 332-0012, Japan*
[7]*Organization for Advanced Studies, Tohoku University, Sendai 980-8577, Japan*
[8]*Institute of Multidisciplinary Research for Advanced Materials, Tohoku University, 2-1-1 Katahira, Sendai, Miyagi 980-8577, Japan*

The spin dynamics of the spin-1/2 kagome-lattice antiferromagnet $Cs_2Cu_3SnF_{12}$ is studied using high-resolution, time-of-flight inelastic neutron scattering. The flat mode, a characteristic of the frustrated kagome antiferromagnet, and the low-energy dispersive mode, which is dominated by magnons, can be well described by the linear spin-wave theory. However, the theory fails to describe three weakly dispersive modes between 9 and 14 meV. These modes could be attributed to two-spinon bound states, which decay into free spinons away from the zone center and at a high temperature, giving rise to continuum scattering.

I. INTRODUCTION

At zero temperature, magnetic moments in a strongly correlated electron system either become ordered [1] or remain disordered but are highly entangled due to quantum correlations [2,3]. The latter is experimentally observed in one-dimensional (1D) systems [4–12] and is well described by the Bethe ansatz [13,14], while the former is ubiquitous in three-dimensional (3D) systems. These two states are believed to be mutually exclusive, and hence, so are their emerging spin dynamics. On the one hand, a highly entangled quantum state gives rise to nonlocal, multiparticle, and fractional $S = 1/2$ excitations called spinons, characterized by a continuum spectrum in neutron scattering [15,16]. On the other hand, the collective excitations of ordered moments result in well-defined, single-particle $S = 1$ excitations called magnons, which can be described by the linear spin-wave theory (LSWT) [17–19]. However, recent studies have revealed the shortcoming of LSWT, which was foreseen by Anderson [18] and Kubo [19] when they first formulated the theory seven decades ago, in describing spin dynamics emerging from classically ordered states in spin-1/2 two-dimensional (2D) edge-sharing triangular [20–24] and square lattices [25].

In a 2D corner-sharing-triangle kagome-lattice antiferromagnet, frustration can destabilize a classical state, and a quantum spin liquid state analogous to that in the 1D systems was theoretically proposed [26–28] and experimentally investigated most intensely for herbertsmithite [29–34]. Even though a majority of the realizations of the kagome-lattice

antiferromagnet are magnetically ordered at low temperatures due to extra terms in the spin Hamiltonian, hints of quantum correlations can still be present in spin dynamics, exposing the limitation of LSWT. In this paper, we demonstrate the breakdown of LSWT in describing spin dynamics emerging from a classical Néel state in the spin-1/2 frustrated kagome-lattice antiferromagnet $Cs_2Cu_3SnF_{12}$.

At room temperature, $Cs_2Cu_3SnF_{12}$ crystallizes in the rhombohedral space group $R\bar{3}m$, where the nearest-neighbor Cu^{2+} ions form a network of the kagome lattice comprising corner-sharing equilateral triangles [35]. A 2D unit cell contains three spins [Fig. 1(a)], with its corresponding Brillouin zone depicted in Fig. 1(c). At $T_s = 185$ K, the compound undergoes a structural phase transition to the monoclinic space group $P2_1/n$, causing a small distortion in the triangles, as shown in Fig. 1(b) [36]. Below $T_N = 20.2$ K, the $S = 1/2$ Cu^{2+} spins order due to the antisymmetric Dzyaloshinskii-Moriya (DM) interaction and weak interlayer coupling, forming the all-in-all-out magnetic structure [37,38] [Fig. 1(a)] with about a one third reduction of the ordered moment [36]. Previous neutron scattering measurements of magnetic excitations revealed a large negative quantum renormalization of the exchange interaction from the high-temperature value, indicative of a significant quantum effect on spin dynamics [39].

This paper is organized as follows. The experiments are discussed in Sec. II. The breakdown of LSWT is demonstrated and discussed in Sec. III A. An analysis of the spin-fluctuation polarization and critical scattering above T_N is given in Sec. III B. In Sec. III C, the existence of spinons and spinon bound states is proposed. Finally, the conclusion is given in Sec. IV.
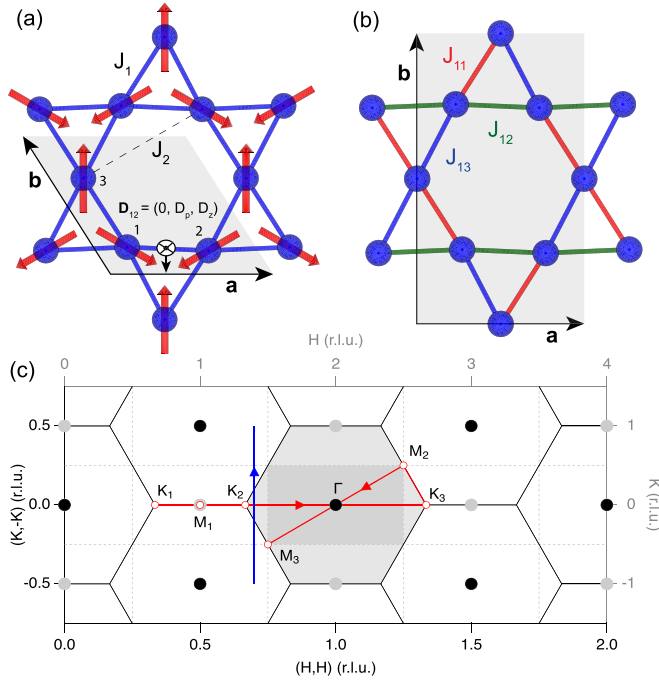
*kittiwit.mat@mahidol.ac.th

FIG. 1. (a) The 2D $R\bar{3}m$ unit cell (shaded area) and the all-in-all-out spin structure are depicted. The uniform exchange interaction J_1 is assumed with one of the next-nearest-neighbor interactions J_2 displayed. The DM vector is shown for one bond, and those for other bonds can be obtained using symmetry operators. (b) The 2D unit cell projected onto the kagome plane for $P2_1/n$ is shown by the shaded area. Three inequivalent exchange interactions are denoted by J_{11}, J_{12}, and J_{13}. (c) The Brillouin zones corresponding to the unit cells in (a) [(b)] are depicted by the hexagonal (rectangular) areas.

II. EXPERIMENTS

Single-crystal $Cs_2Cu_3SnF_{12}$ was synthesized using a method described in Ref. [35]. Magnetic excitations in $Cs_2Cu_3SnF_{12}$ were measured on the cold-neutron time-of-flight disk-chopper spectrometer Amateras [40] at the Japan Proton Accelerator Research Complex. The sample, which consisted of three coaligned single crystals with a total mass of 3.82 g, was aligned so that the [110] and [001] directions were horizontal and in the scattering plane. Reciprocal lattice vectors throughout this paper are given in the rhombohedral space group $R\bar{3}m$ of the high-temperature phase, where the 2D magnetic unit cell is denoted by the shaded area in Fig. 1(a), with lattice parameters $a = 7.105$ and $c = 20.381$ Å, and the corresponding Brillouin zone is shown by the solid lines in Fig. 1(c). The sample was loaded into an aluminum can and cooled down to a base temperature of 7 K using a closed-cycle ^{4}He cryostat. The monochromator disk choppers rotated at 150 Hz with 30 mm width slits and two different conditions for choppers (including auxiliary choppers) to select two different setups of incident energies of (i) 4.0, 6.4, 11.7, and 27.6 meV and (ii) 5.0, 8.4, 17.0, and 51.0 meV. We found that an incident energy of 17.0 meV gives the optimal results in terms of dynamic-range coverage and the incident neutron flux. A resolution of the incident energy of 5.0 meV is sufficient to resolve the magnetic-anisotropy gap of 0.7 meV at the magnetic zone center. Multiple data sets were acquired by rotating the sample about the vertical axis, which is parallel to the $(\bar{1}10)$ direction, in a step of $2°$ covering roughly $100°$ of the sample orientation. The magnetic excitations were measured at the base temperature and 30 K, which is about 10 K above T_N, while the phonon background was measured at 150 K. These data were processed using the software package UTSUSEMI [41] to generate the four-dimensional scattering intensity data $I(\mathbf{Q}, \hbar\omega)$, where $\mathbf{Q}$ is the momentum transfer and $\hbar\omega$ is the energy transfer. The obtained data were then sliced and cut along high-symmetry directions to produce scattering intensity maps and line scans. Taking advantage of the nondispersive and rodlike scattering along the direction perpendicular to the kagome plane, which results from the two-dimensionality of the system, we integrate the intensity along the [001] direction to increase a signal-to-background ratio. To avoid phonon contributions, the L integration for most of the figures was taken for an L range of $[-3, 3]$ reciprocal lattice units (r.l.u.) except for the H-K maps, for which the integration was taken for the whole measured L range.

III. RESULTS AND DISCUSSION

A. Breakdown of linear spin-wave theory

The measured scattering intensity map as a function of energy transfer ($\hbar\omega$) and momentum transfer measured at 7 K along high-symmetry directions, illustrated by the red lines in Fig. 1(c), displays the energy spectrum of spin dynamics up to 15 meV. We first attempt to describe the magnetic excitations using LSWT. Spin-wave calculations are based on the all-in-all-out spin structure with a uniform nearest-neighbor exchange interaction J_1 [Fig. 1(a)]. The lattice distortion, which results in the nonuniformity of the exchange interactions, is very small [35,36]. Hence, the distortion-induced, spatially anisotropic exchange interactions are ignored. To first approximation, the spin Hamiltonian is given by

$$\mathcal{H} = \sum_{\langle i,j \rangle}[J_1\mathbf{S}_i \cdot \mathbf{S}_j + \mathbf{D}_{ij} \cdot (\mathbf{S}_i \times \mathbf{S}_j)] + \sum_{\langle l,k \rangle}J_2\mathbf{S}_l \cdot \mathbf{S}_k,$$

where J_1 and J_2 are the nearest- and next-nearest-neighbor interactions, respectively, and $\mathbf{D}_{ij}$ denotes the DM vector between the nearest-neighbor spins. $\mathbf{D}_{12} = (0, D_p, D_z)$ is shown in Fig. 1(a), and all other DM vectors can be obtained by symmetry operators. The dominance of the DM interaction in selecting and stabilizing the all-in-all-out spin structure results in a robust spin structure against the small differences in the spatially anisotropic exchange. Hence, the LSWT calculations for the enlarged 2D magnetic unit cell with six spins including the spatially anisotropic exchange interactions, which will be discussed later, do not show any improvement in explaining the data compared with the uniform-exchange-interaction model.

The spin-wave calculations exhibit three transverse magnon modes, two of which, the "weather vane" (flat) [42–44] and dispersive low-energy modes, were fitted to the measured dispersion to obtain D_z and J_1, respectively. The weakly dispersive nature of the flat mode is a result of ferromagnetic J_2. D_p, which determines the spin-wave anisotropic gap at the zone center [see Fig. 7(a) below], was fit to reproduce this gap energy. The best fit denoted by the red line in Fig. 2(a) yields fit parameters $J_1 = 13.3(2)$, $J_2 = -0.24(6)$,
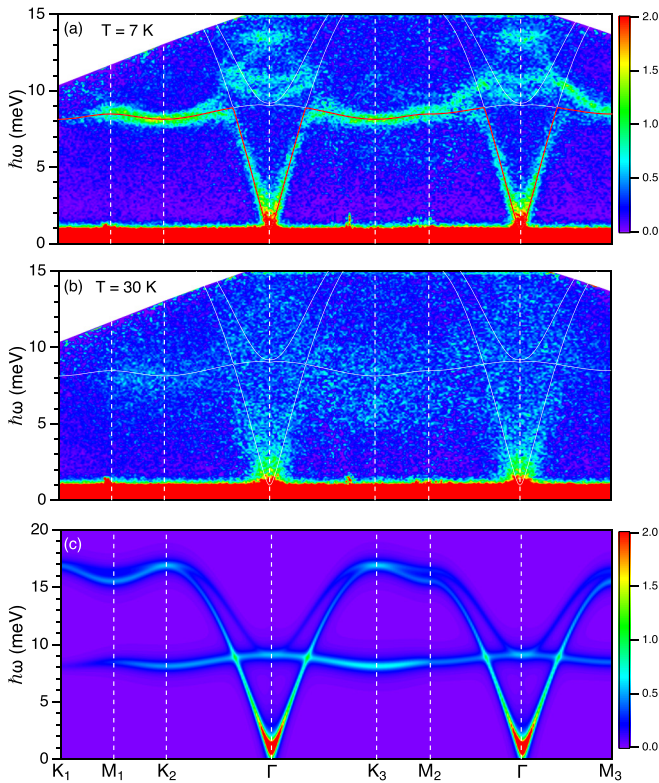
FIG. 2. Measured scattering intensity maps as a function of the momentum transfer and energy transfer show the magnetic excitation spectrum at (a) 7 and (b) 30 K along the high-symmetry directions, which are depicted by the red lines in Fig. 1(c). For comparison, the calculated intensity map based on LSWT along the same directions is shown in (c).

$D_p = 0.566(2)$, and $D_z = -1.94(8)$ meV. The value of J_1 represents the renormalization factor of 0.67, consistent with a previous work [39]. The spin-wave results [see Figs. 2(a) and 2(c)] can capture the low-energy part of the resolution-limited, single-particle magnetic excitations up to the flat mode around 8 meV. However, it fails to reproduce the full spectrum. Comparing the measured dispersion in Fig. 2(a) and the calculated one in Fig. 2(c), we highlight the inconsistencies in (i) the absence of the flat mode around the zone center, (ii) the absence of the high-energy dispersive modes around the *M* and *K* points (see also Figs. 2(a) and 2(b) in Ref. [45]), (iii) three weakly dispersive, resolution-limited modes centered at 9.6(2), 10.7(1), and 13.4(1) meV measured at the Γ point, as shown in Fig. 3, and (iv) broad scattering around the flat mode [see also Fig. 5(a) below]. Furthermore, we note that even though LSWT appears to well reproduce the lower branch of the flat mode along the zone edges, it fails to capture the branching out to high energy near the zone center, as observed in Fig. 2(a) [see also Fig. 5(a) below], which suggests the existence of another mode beyond LSWT.

The failure of the linear spin-wave theory is further highlighted in the constant-energy intensity maps shown in Fig. 4. The low-energy spin dynamics shown as a ring of scattering intensity in Fig. 4(a) originates from the hexagonal zone centers and is well reproduced by LSWT, as shown in Fig. 4(g). The agreement between the measured and calculated magnetic excitations persists up to around 8 meV, where the flat
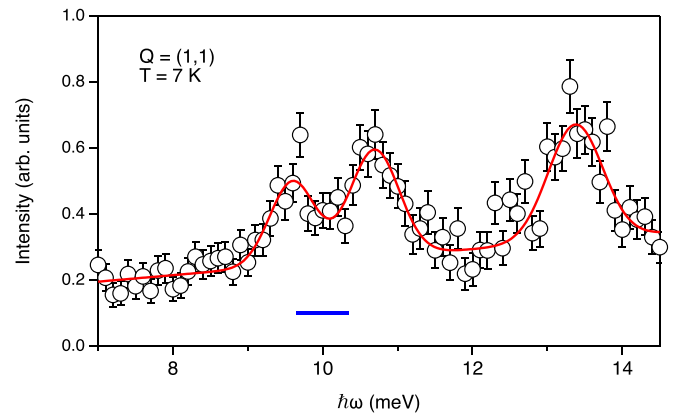

FIG. 3. An energy cut through the zone center at 7 K shows the three weakly dispersive modes centered at 9.6(2), 10.7(1), and 13.4(1) meV. The red curve denotes a fit to three Gaussians. The horizontal blue line denotes the energy resolution measured at the elastic position.

mode was observed, when comparing Fig. 4(b) with Fig. 4(h). The high intensity at the zone corner at $\hbar\omega = 8$ meV where three Brillouin zones meet is consistent with the high-intensity region obtained in the calculations. However, above 8 meV the measured and calculated results appear to be significantly different from each other, as shown in Figs. 4(c)–4(f) and 4(i)–4(l), respectively. Figure 4(c) shows a ring of scattering intensity around the zone corner at 9 meV. This ring becomes larger at 10 meV, and the scattering intensity forms an X pattern at the zone centers [Fig. 4(d)]. On the other hand, the calculated results show that most of the scattering intensity remains centered around the zone centers at 9 and 10 meV [Figs. 4(i) and 4(j)]. At 11 meV, while the calculated scattering intensity forms a spherical profile around the zone centers [Fig. 4(k)], the measured scattering intensity forms a nonspherical, starlike shape, as shown in Fig. 4(e). Finally, at 14 meV most of the measured intensity appears around the zone centers [Fig. 4(f)], while at 15 meV the calculated scattering intensity is absent around the zone center and, instead, is present near the zone edges [Fig. 4(l)]. This discrepancy highlights the failure of LSWT to describe the magnetic excitations in $Cs_2Cu_3SnF_{12}$ at energies above the flat mode.

The most conspicuous discrepancy between the measured dispersion and LSWT is the existence of the three weakly dispersive modes around the zone center between 9 and 14 meV. The spin-wave calculations predict only one highly dispersive magnon mode starting from 9.2 meV at the Γ point and reaching 16.9 meV at the *K* point [Fig. 2(c)]. Unlike the flat and dispersive low-energy modes, which have some parts that agree with the measured dispersion, this magnon mode is entirely absent. Instead, it is replaced by three weakly dispersive modes, which quickly terminate away from the zone center. The termination wave vector approaches the zone center for the higher-energy modes, forming a profile resembling the top of a pyramid [Fig. 2(a)]. We note that these modes were not observed in the spin-5/2 kagome-lattice antiferromagnet $KFe_3(OH)_6(SO_4)_2$ (jarosite) [46] despite both having the same classical all-in-all-out ordered state, suggesting the manifestation of the quantum effect on spin dynamics in $Cs_2Cu_3SnF_{12}$.
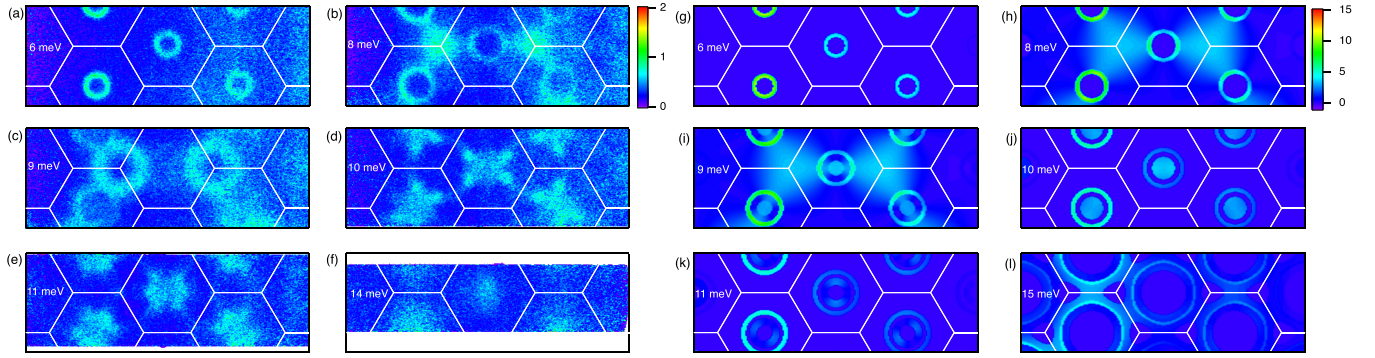
FIG. 4. Scattering intensity maps at a constant energy as a function of in-plane momenta (*H*-*K* plane) measured at 7 K for (a) 6, (b) 8, (c) 9, (d) 10, (e) 11, and (f) 14 meV. For comparison, scattering intensity maps at a constant energy as a function of in-plane momenta were also calculated based on LSWT for (g) 6, (h) 8, (i) 9, (j) 10, (k) 11, and (l) 15 meV.

Another distinct feature of the measured dispersion that cannot be reproduced by LSWT is the broad scattering around the flat mode, which is most evident in the intensity map along the $[K, -K]$ direction centered at (0.7,0.7), as shown in Figs. 5(a) and 5(c) for 7 K and 30 K, respectively. This broad intensity is highlighted in the integrated intensity as a function of energy by the red solid lines in Figs. 5(b) and 5(d). The onset of the broad intensity, which extends up to 12 meV, starts around 2 meV. At 7 K (30 K), it peaks at 8.9(2) [8.0(1)] meV, nearly coinciding with the flat mode centered at 8.32(1) [8.2(1)] meV. The proximity of the single-particle flat mode to the broad scattering could hint at their interconnection.

B. Spin-fluctuation polarization and critical scattering above T_N

Analysis of the spin-fluctuation polarization was performed for the low-energy dispersive mode, flat mode, and three modes between 9 and 14 meV. The polarization factor in the magnetic scattering cross section is governed by $f(Q)^2[1 \pm (Q_L/Q)^2]$, where $f(Q)$ is the Cu^{2+} magnetic form factor, the positive (negative) sign is for in-plane (out-of-plane) polarization, and Q_L (Q) denotes the L component (magnitude) of **Q**. Figures 6(a), 6(c), 6(e), and 6(g) show the constant-energy contour maps in the (H, H, L) plane, where magnetic scattering forms a rod along L attesting to the two-dimensionality of the spin network. We note that within the resolution of the spectrometer, the energy dispersion along L is flat (not shown), and hence, the interplanar coupling ($J_\perp$) cannot be extracted from our inelastic neutron scattering data. A rough estimate using the energy resolution yields the upper limit of $J_\perp$ at $\sim 0.05 J_1$. For comparison, $J_\perp$ in jarosite estimated from the magnetization [47] and electron spin resonance [48] measurements is one order of magnitude smaller than this upper-limit value.
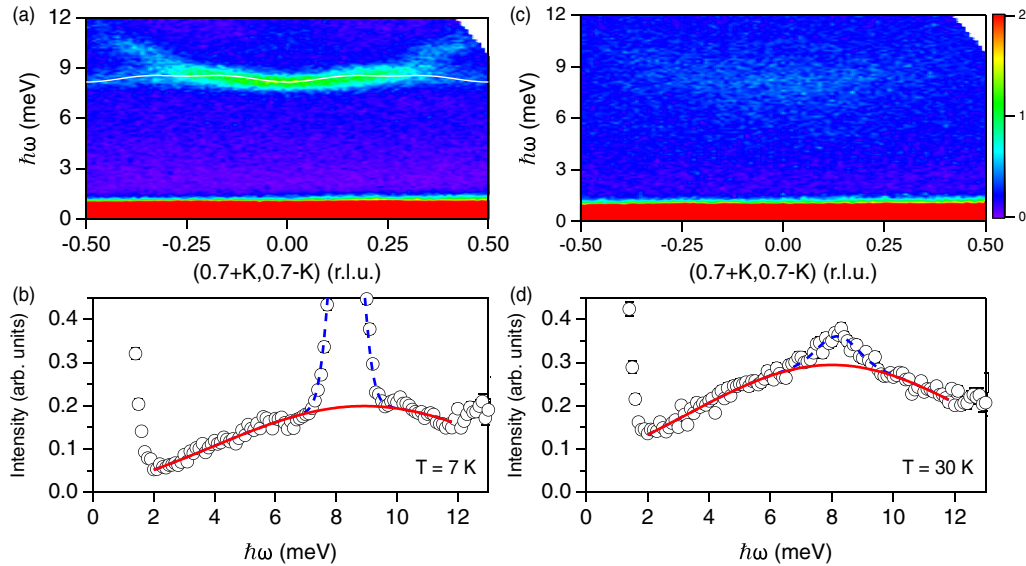

FIG. 5. Temperature dependence of the flat mode and broad scattering around the flat mode. Scattering intensity maps as a function of energy and momentum transfer along $(K, -K)$ centered at (0.7,0.7) as shown by the blue line in Fig. 1(c) were measured at (a) 7 and (c) 30 K. The integrated scattering intensity $[(H, H) = (0.6, 0.6)$ to $(0.8,0.8)$ r.l.u. and $(K, -K) = (-0.25, 0.25)$ to $(0.25, -0.25)$ r.l.u.] as a function of energy is shown in (b) and (d) for 7 and 30 K, respectively. The solid line in (a) shows the LSWT result. In (b) and (d), the red solid lines denote fits to a Gaussian for the broad scattering, and the dashed blue lines show the flat mode.
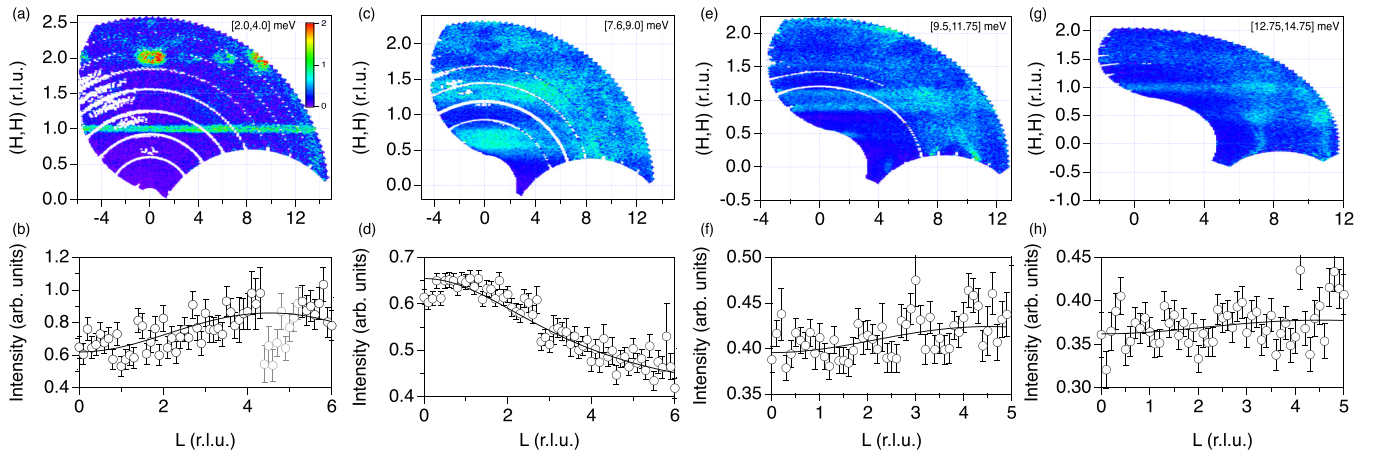
FIG. 6. Scattering intensity maps as a function of (H, H) and L measured at 7 K show rodlike scattering intensity along L for the integrated energy ranges (a) [2.0, 4.0], (c) [7.6, 9.0], (e) [9.5, 11.75], and (g) [12.75, 14.75] meV. (b), (d), (f), and (h) show integrated intensity as a function of L. The integrated ranges for (H, H) are (b) (0.95, 0.95) to (1.05,1.05), (d) (0.450, 0.450) to (0.825,0.825), (f) (0.8, 0.8) to (1.2,1.2), and (h) (0.9, 0.9) to (1.1,1.1) r.l.u. Solid lines in (b), (d), (f), and (h) denote fits to the polarization factor described in the text.

The integrated intensity along the scattering rod as a function of L for the low-energy dispersive mode [Fig. 6(b)] reveals the in-plane polarization, consistent with the fact that the anisotropic gap at the bottom of this mode [Fig. 7(a)] results from the in-plane component D_p of the DM vector, which functions as effective easy-axis anisotropy. On the other hand, as shown in Fig. 6(d), the flat mode is out of plane polarized, confirming its connection to the out-of-plane component D_z, which functions as effective easy-plane anisotropy. The polarizations of the three modes around the zone center [see Fig. 6(f) for the two modes at 9.6 and 10.7 meV and Fig. 6(h) for the 13.41 meV mode] suggest that they are

in plane polarized, which could indicate that these modes are longitudinal modes given that quasiparticles are confined within the kagome plane. The polarization analysis appears to suggest that the in-plane modes exist only around the zone center, while the out-of-plane mode disappears near the zone center but prevails near the zone edges. Furthermore, while the calculated spin-wave results indicate that the out-of-plane-polarized flat mode attains high intensity throughout the Brillouin zone and the in-plane-polarized dispersive mode survives up to high energies [Fig. 2(c)], the data [Fig. 2(a)] show that both modes terminate where they cross each other.
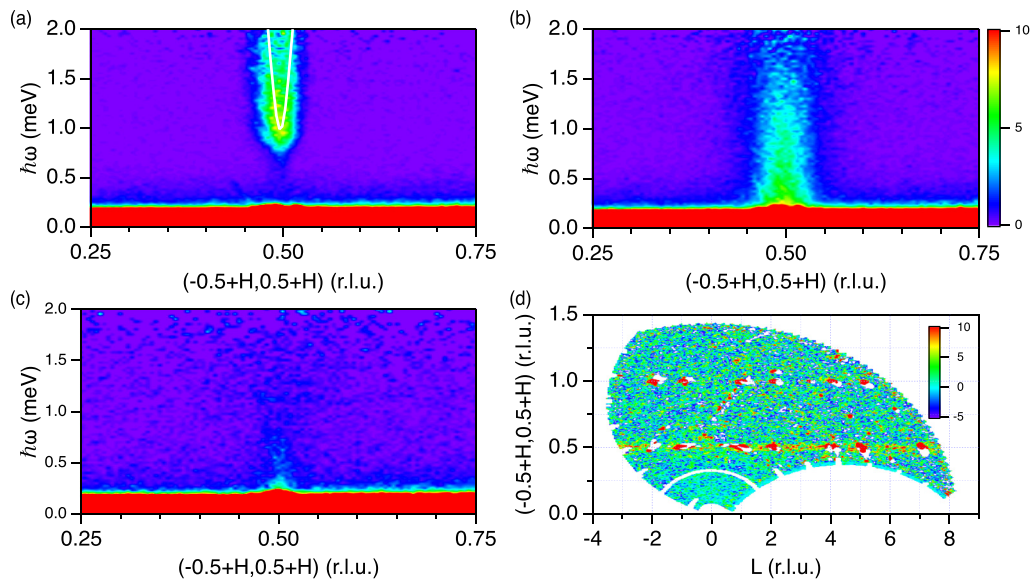

FIG. 7. Temperature dependence of the spin-anisotropic energy gap. Scattering intensity maps as a function of energy and momentum transfer along (H, H) centered at $(0,1)$ show (a) the energy gap at 7 K, (b) the closing of the gap at 30 K with the remnant scattering intensity at low energy, and (c) the disappearance of the remnant scattering at 150 K. The solid line in (a) denotes the LSWT result. In (d), the difference map between the integrated quasielastic intensity $I_{q\text{-el}}$ (an integrated energy range of $[-0.5, 0.5]$ meV) measured at 30 and 7 K $[I_{q\text{-el}}(30 \text{ K}) - I_{q\text{-el}}(7 \text{ K})]$ shows the scattering rod at $(0,1)$ along L.

At 30 K, about 10 K above T_N, the resolution-limited, single-particle excitations of the low-energy dispersive mode and flat mode, which is dominant near the zone edges, disappear and are replaced by a column of continuum scattering [Figs. 2(b) and 7(b)] and a broad peak [indicated by the dashed blue line in Fig. 5(d)], respectively. The remnant broad scattering of the flat mode, which remains centered around 8 meV, implies that spins are confined to fluctuate within the kagome plane and retain two-dimensional rotational symmetry in the plane, while the closing of the in-plane anisotropy gap [Fig. 7(b)] suggests that spins can freely rotate in the plane. Furthermore, due to the effect of the out-of-plane DM interaction, which determines spin chirality, the in-plane fluctuations, which form a scattering rod along L [as shown in Fig. 7(d)] and disappear at 150 K [Fig. 7(c)], must preserve the chirality of the ordered state. Therefore, above T_N, the system transitions into a chiral ordered state with the absence of rotational symmetry breaking. This chiral state was previously observed in jarosite [49]. The low-energy spin fluctuations resulting in the quasielastic scattering observed in Figs. 7(b) and 7(d) can be associated with a critical phenomenon of the ordered moments at the magnetic phase transition, supporting the dominance of magnons at low energy, which could also explain why LSWT works exceptionally well in this regime.

C. Possible existence of spinons and spinon bound states

As previously discussed in Sec. III A, LSWT alone cannot fully describe spin dynamics in $Cs_2Cu_3SnF_{12}$. We can also rule out the effect of the doubling of the magnetic unit cell due to the structural transition at T_s because the "ghost mode" [45] resulting from the zone folding, which was also observed in the cousin compound $Rb_2Cu_3SnF_{12}$ [50–52], cannot describe the discrepancies. Specifically, the enlarged magnetic unit cell resulting from the structural phase transition from $R\bar{3}m$ to $P2_1/n$ cannot explain the magnetic excitation spectrum above the flat mode. Figure 8(a) shows the calculated spin-wave spectrum based on the enlarged 2D magnetic cell containing six spins [Fig. 1(b)]. This enlarged magnetic cell is the projection of a monoclinic unit cell in space group $P2_1/n$ onto the kagome plane. The enlarged unit cell gives rise to the folding of the Brillouin zone, as evidenced by an extra low-energy dispersive mode originating from the M point in the calculated spin waves and experimental data, as indicated by the arrows in Figs. 8(a) and 8(b), respectively. We note that this ghost mode is not observed in Fig. 2(a), where the measurements were done using the incident neutron energy E_i of 17 meV, and that it is only faintly visible in Fig. 8(a) using neutrons with E_i of 11.7 meV, where the neutron flux is higher and hence yields a better signal-to-noise ratio than that with E_i of 17 meV. The scattering intensity of this ghost mode at the M points is much smaller than the low-energy dispersive mode at the zone centers due to the all-in-all-out magnetic structure, which yields weak magnetic scattering intensity at the M points. The LSWT result also shows that the folding does not give rise to the three modes between 9 and 14 meV around the Γ point, as evidenced by the absence of spin-wave branches between 10 and 15 meV [Fig. 8(a)]. Furthermore, varying the relative values of the spatially anisotropic nearest-neighbor interactions J_{11}, J_{12}, and J_{13} does not resolve the inconsistency
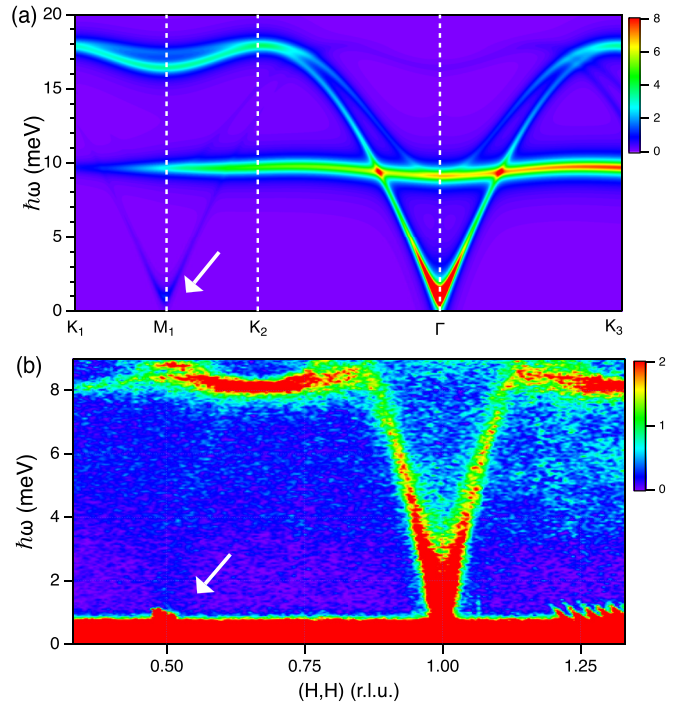

FIG. 8. (a) The scattering intensity map as a function of momentum and energy shows the calculated spin-wave spectrum using LSWT based on the enlarged 2D unit cell. We note that the structural phase transition gives rise to a total of three domains, whereas Fig. 1(b) shows only a single domain. Hence, the "ghost-mode" excitations will appear at all M points [45]. (b) The scattering intensity map was measured using an incident neutron energy of 11.7 meV at 7 K. The arrows indicate the ghost mode.

between the calculated spin waves and experimental data. In particular, it cannot reproduce the three high-intensity, weakly dispersive modes between 9 and 14 meV.

Another explanation which includes higher-order (cubic and quartic) terms in the spin-wave expansion was examined in Ref. [53], where the absence or broadening of the dispersive excitations above the flat mode in the kagome antiferromagnet can be explained by a decay of the quasiparticle into two magnons belonging to the flat mode, which is possible for a noncollinear system. However, this scenario also fails to capture the loss of intensity of the dispersive and flat modes after their crossing, as observed in Fig. 2(a). Given that the energy of the flat mode is around 8 meV, one would expect the dispersive mode to become broadened around 16 meV, which is twice the flat-mode energy. However, from the data, we start to observe the loss of intensity of the dispersive mode above 9 meV. Furthermore, this model is unable to explain the three weakly dispersive modes around the zone center. These modes do not resemble any of the calculated spin-wave modes, and hence, their origin is most likely not due to a minor improvement of the spin-wave theory such as the inclusion of higher-order terms in the spin-wave expansion. The fact that the peak profile of these excitations is resolution limited (Fig. 3) suggests that they do not result from the broadening of the magnon modes. We believe that these modes correspond to two-spinon bound states (triplons) [54,55], which could decay into free spinons away from the zone center.

At 30 K, these modes also decay, forming continuum scattering extending up to 15 meV (the highest measuring energy) [Fig. 2(b)]. The spinon continuum at 30 K retains the profile shaped like the top of a pyramid, suggesting energy conservation of the decay. Furthermore, the upper branch of the flat mode, which disperses to high energy close to the zone center, could also be attributed to the triplons, and the decay of these triplons at 30 K could increase the continuum intensity around the flat mode [compare the red lines in Figs. 5(b) and 5(d)]. The fact that the center of the continuum at 30 K is roughly the same as the energy of the flat mode suggests an energy-conserving decay of the triplons into free spinons. In addition, it was recently reported that the continuum also exists up to 50 meV [45], substantiating the existence of free spinons at high energy. Therefore, we conjecture that the triplons are dominant around the zone center between 9 and 14 meV and that they become unstable and decay into free spinons away from the zone center, at high energy, or at high temperature. It is not clear what interaction can bind pairs of spinons to form triplons. In a spatially anisotropic triangular antiferromagnet, it was shown that a pair of spinons can lower their kinetic energy by forming a triplon that propagates between chains [54].

In $Cs_2Cu_3SnF_{12}$, the existence of spinons and their bound states could be attributed to the one third of magnetic moments that remain disordered at low temperature and possibly form an entangled quantum state, whereas the dominance of magnons at low energy could be the contributions from the two thirds of the magnetic moments that order. In the triangular- and square-lattice spin-1/2 antiferromagnets [20,22,23,25], the deviation of the observed magnetic excitation spectrum from the result of LSWT was also observed. To explain the excitation spectra in these systems, a fermionic resonating valence-bond theory was proposed, and single-particle spin dynamics arises as the two-spinon bound state [25,56,57]. A similar mechanism could also play a key role in the spin dynamics of the spin-1/2 kagome antiferromagnet. A recent large-scale numerical calculation using a tensor network renormalization group method captured all key features of the spin-dynamic spectra of the triangular-lattice antiferromagnet [58] and could be applied to the kagome system.

IV. CONCLUSION

We have performed high-resolution, time-of-flight inelastic neutron scattering and mapped out the magnetic excitations in the kagome-lattice antiferromagnet $Cs_2Cu_3SnF_{12}$. Low-energy spin dynamics can be well described by LSWT. However, the theory becomes inadequate to describe the whole energy spectrum. We observed the disappearance of the flat-mode intensity near the zone center, the absence of the dispersive modes around the M and K points, the emergence of extra modes between 9 and 14 meV, and a broad continuum around the flat mode, all of which cannot be accounted for by LSWT. Our results reveal a shortfall of the semiclassical framework, which has been ubiquitously used to describe the spin dynamics of a magnetically ordered system, in describing magnetic excitations in this 2D frustrated kagome system. The breakdown of LSWT necessitates a new quantum-based theoretical framework to describe spin dynamics in $Cs_2Cu_3SnF_{12}$ and other magnetically ordered 2D systems.

ACKNOWLEDGMENTS

[1] M. L. Néel, Ann. Phys. (Berlin, Ger.) **12**, 137 (1948).

[2] P. A. M. Dirac, *The Principles of Quantum Mechanics* (Oxford University Press, Oxford, 1947).

[3] P. W. Anderson, Mater. Res. Bull. **8**, 153 (1973).

[4] S. E. Nagler, D. A. Tennant, R. A. Cowley, T. G. Perring, and S. K. Satija, Phys. Rev. B **44**, 12361 (1991).

[5] B. Lake, D. A. Tennant, and S. E. Nagler, Phys. Rev. Lett. **85**, 832 (2000).

[6] B. Lake, D. A. Tennant, C. D. Frost, and S. E. Nagler, Nat. Mater. **4**, 329 (2005).

[7] R. Coldea, D. A. Tennant, A. M. Tsvelik, and Z. Tylczynski, Phys. Rev. Lett. **86**, 1335 (2001); R. Coldea, D. A. Tennant, and Z. Tylczynski, Phys. Rev. B **68**, 134424 (2003).

[8] T. Ono, H. Tanaka, H. Aruga Katori, F. Ishikawa, H. Mitamura, and T. Goto, Phys. Rev. B **67**, 104431 (2003).

[9] M. Mourigal, M. Enderle, A. Klöpperpieper, J.-S. Caux, A. Stunault, and H. M. Rønnow, Nat. Phys. **9**, 435 (2013).

[10] T. Nikuni, M. Oshikawa, A. Oosawa, and H. Tanaka, Phys. Rev. Lett. **84**, 5868 (2000); A. Oosawa, M. Ishii, and H. Tanaka, J. Phys.: Condens. Matter **11**, 265 (1999).

[11] C. Rüegg, N. Cavadini, A. Furrer, H.-U. Güdel, K. Krämer, H. Mutka, A. Wildes, K. Habicht, and P. Vorderwisch, Nature (London) **423**, 62 (2003).

[12] M. Enderle, B. Fak, H.-J. Mikeska, R. K. Kremer, A. Prokofiev, and W. Assmus, Phys. Rev. Lett. **104**, 237207 (2010).

[13] H. Bethe, Z. Phys. **71**, 205 (1931).

[14] B. Lake, D. A. Tennant, J.-S. Caux, T. Barthel, U. Schollwöck, S. E. Nagler, and C. D. Frost, Phys. Rev. Lett. **111**, 137205 (2013).

[15] L. D. Faddeev and L. A. Takhtajan, Phys. Lett. A **85**, 375 (1981).

[16] F. D. M. Haldane, Phys. Rev. Lett. **66**, 1529 (1991).

[17] L. Hulthèn, Ark. Mat. Astron. Fys. A **26**, 1 (1938).

[18] P. Anderson, Phys. Rev. **86**, 694 (1952).

[19] R. Kubo, Phys. Rev. **87**, 568 (1952).

[20] J. Ma, Y. Kamiya, T. Hong, H. B. Cao, G. Ehlers, W. Tian, C. D. Batista, Z. L. Dun, H. D. Zhou, and M. Matsuda, Phys. Rev. Lett. **116**, 087201 (2016).

[21] T. Susuki, N. Kurita, T. Tanaka, H. Nojiri, A. Matsuo, K. Kindo, and H. Tanaka, Phys. Rev. Lett. **110**, 267201 (2013).

[22] Y. Kamiya, L. Ge, T. Hong, Y. Qiu, D. L. Quintero-Castro, Z. Lu, H. B. Cao, M. Matsuda, E. S. Choi, C. D. Batista, M. Mourigal, H. D. Zhou, and J. Ma, Nat. Commun. **9**, 2666 (2018).

[23] S. Ito, N. Kurita, H. Tanaka, S. Ohira-Kawamura, K. Nakajima, S. Itoh, K. Kuwahara, and K. Kakurai, Nat. Commun. **8**, 235 (2017).

[24] D. Macdougal, S. Williams, D. Prabhakaran, R. I. Bewley, D. J. Voneshen, and R. Coldea, Phys. Rev. B **102**, 064421 (2020).

[25] B. Dalla Piazza, M. Mourigal, N. B. Christensen, G. J. Nilsen, P. Tregenna-Piggott, T. G. Perring, M. Enderle, D. F. Mcmorrow, D. A. Ivanov, and H. M. Ronnow, Nat. Phys. **11**, 62 (2015).

[26] L. Balents, Nature (London) **464**, 199 (2010).

[27] L. Savary and L. Balents, Rep. Prog. Phys. **80**, 016502 (2017).

[28] C. Broholm, R. J. Cava, S. A. Kivelson, D. G. Nocera, M. R. Norman, and T. Senthil, Science **367**, eaay0668 (2020).

[29] M. Shores, E. Nytko, B. Bartlett, and D. G. Nocera, J. Am. Chem. Soc. **127**, 13462 (2005).

[30] P. Mendels, F. Bert, M. A. deVries, A. Olariu, A. Harrison, F. Duc, J. C. Trombe, J. S. Lord, A. Amato, and C. Baines, Phys. Rev. Lett. **98**, 077204 (2007).

[31] J. S. Helton, K. Matan, M. P. Shores, E. A. Nytko, B. M. Bartlett, Y. Yoshida, Y. Takano, A. Suslov, Y. Qiu, J.-H. Chung, D. G. Nocera, and Y. S. Lee, Phys. Rev. Lett. **98**, 107204 (2007).

[32] T.-H. Han, J. S. Helton, S. Chu, D. G. Nocera, J. A. Rodriguez-Rivera, C. Broholm, and Y. S. Lee, Nature (London) **492**, 406 (2012).

[33] M. R. Norman, Rev. Mod. Phys. **88**, 041002 (2016).

[34] D. Inosov, Adv. Phys. **67**, 149 (2018).

[35] T. Ono, K. Morita, M. Yano, H. Tanaka, K. Fujii, H. Uekusa, Y. Narumi, and K. Kindo, Phys. Rev. B **79**, 174407 (2009).

[36] K. Matan, T. Ono, G. Gitgeatpong, K. de Roos, P. Miao, S. Torii, T. Kamiyama, A. Miyata, A. Matsuo, K. Kindo, S. Takeyama, Y. Nambu, P. Piyawongwatthana, T. J. Sato, and H. Tanaka, Phys. Rev. B **99**, 224404 (2019).

[37] A. S. Wills, A. Harrison, C. Ritter, and R. I. Smith, Phys. Rev. B **61**, 6156 (2000).

[38] M. Nishiyama, S. Maegawa, T. Inami, and Y. Oka, Phys. Rev. B **67**, 224435 (2003).

[39] T. Ono, K. Matan, Y. Nambu, T. J. Sato, K. Katayama, S. Hirata, and H. Tanaka, J. Phys. Soc. Jpn. **83**, 043701 (2014).

[40] K. Nakajima *et al.*, J. Phys. Soc. Jpn. **80**, SB028 (2011).

[41] Y. Inamura, T. Nakatani, J. Suzuki, and T. Otomo, J. Phys. Soc. Jpn. **82**, SA031 (2013).

[42] S. Sachdev, Phys. Rev. B **45**, 12377 (1992).

[43] A. B. Harris, C. Kallin, and A. J. Berlinsky, Phys. Rev. B **45**, 2899 (1992).

[44] D. A. Huse and A. D. Rutenberg, Phys. Rev. B **45**, 7536 (1992).

[45] M. Saito, R. Takagishi, N. Kurita, M. Watanabe, H. Tanaka, R. Nomura, Y. Fukumoto, K. Ikeuchi, and R. Kajimoto, Phys. Rev. B **105**, 064424 (2022).

[46] K. Matan, D. Grohol, D. G. Nocera, T. Yildirim, A. B. Harris, S. H. Lee, S. E. Nagler, and Y. S. Lee, Phys. Rev. Lett. **96**, 247201 (2006).

[47] K. Matan, B. M. Bartlett, J. S. Helton, V. Sikolenko, S. Matas, K. Prokes, Y. Chen, J. W. Lynn, D. Grohol, T. J. Sato, M. Tokunaga, D. G. Nocera, and Y. S. Lee, Phys. Rev. B **83**, 214406 (2011).

[48] T. Fujita, H. Yamaguchi, S. Kimura, T. Kashiwagi, M. Hagiwara, K. Matan, D. Grohol, D. G. Nocera, and Y. S. Lee, Phys. Rev. B **85**, 094409 (2012).

[49] D. Grohol, K. Matan, J. Cho, S.-H. Lee, J. W. Lynn, D. Nocera, and Y. S. Lee, Nat. Mater. **4**, 323 (2005).

[50] K. Morita, M. Yano, T. Ono, H. Tanaka, K. Fujii, H. Uekusa, Y. Narumi, and K. Kindo, J. Phys. Soc. Jpn. **77**, 043707 (2008).

[51] K. Matan, T. Ono, Y. Fukumoto, T. J. Sato, J. Yamaura, M. Yano, K. Morita, and H. Tanaka, Nat. Phys. **6**, 865 (2010).

[52] K. Matan, Y. Nambu, Y. Zhao, T. J. Sato, Y. Fukumoto, T. Ono, H. Tanaka, C. Broholm, A. Podlesnyak, and G. Ehlers, Phys. Rev. B **89**, 024414 (2014).

[53] A. L. Chernyshev, Phys. Rev. B **92**, 094409 (2015); A. L. Chernyshev and M. E. Zhitomirsky, *ibid.* **92**, 144415 (2015).

[54] M. Kohno, O. A. Starykh, and L. Balents, Nat. Phys. **3**, 790 (2007).

[55] K. Nawa, D. Hirai, M. Kofu, K. Nakajima, R. Murasaki, S. Kogane, M. Kimata, H. Nojiri, Z. Hiroi, and T. J. Sato, Phys. Rev. Research **2**, 043121 (2020).

[56] F. Ferrari and F. Becca, Phys. Rev. X **9**, 031026 (2019).

[57] C. Zhang and T. Li, Phys. Rev. B **102**, 075108 (2020).

[58] R.-Z. Chi, Y. Liu, Y. Wan, H.-J. Liao, and T. Xiang, arXiv:2201.12121.